



Capturing the inter-particle force distribution in granular material using LS-DEM

Liuchi Li¹ · Eloïse Marteau¹ · José E. Andrade¹

Received: 1 November 2018 / Published online: 17 May 2019
© Springer-Verlag GmbH Germany, part of Springer Nature 2019

Abstract

Particle shape, as one of the most important physical ingredients of granular materials, can greatly alter the characteristic of inter-particle force distribution which is of vital importance in understanding the mechanical behavior of granular materials. However, currently both experimental and numerical studies remain limited in this regard. In this paper, we for the first time validate the ability of the level set discrete element method (LS-DEM) on capturing the inter-particle force distribution among particles of arbitrary shape. We first present the technical detail of LS-DEM; we then apply LS-DEM to simulate experiments of shearing granular materials composed of arbitrarily shaped particles. The proposed approach directly links experimentally measured material properties to model parameters such as contact stiffness without any calibration. Our results show that LS-DEM is able to not only capture the macro scale response such as stress and deformation, but also to reproduce the particle scale contact information such as the distribution of contact force magnitude, contact orientation and contact friction mobilization. Our work demonstrates the promising potential of LS-DEM on studying the mechanics and physics of natural granular material and on aiding design granular particle shape for novel macro-scale mechanical property.

Keywords Contact forces · Discrete element method · Validation · Force measurement

1 Introduction

Any collection of macroscopic solid frictional particles with size greater than $1\ \mu\text{m}$ belong to the family of granular materials. They are ubiquitous on earth and are the second most manipulated industrial material [1]. Despite such a unified and simple definition, at the macro-scale, different granular materials can exhibit drastically different mechanical properties and can behave like solids, liquids, gas or even with the aforementioned phases coexisting [2, 3] under different external loading and boundary setting. Such complex macro-scale behavior is closely tied to the heterogeneously distributed force chains formed by inter-particle forces [4, 5], the characteristic of which is sensitive to particle shape effect [6, 7]. However, investigations on the force transmission among arbitrarily shaped particles are still lacking due to several technical limitations both experimentally and computationally. On one hand, most experimental studies so far

involving measuring inter-particle forces rely on advanced optical techniques (for example refractive index matching tomography [8] and 3D X-ray diffraction and X-ray tomography [9]) that are able to reasonably measure particle scale deformation. Because of this, these methods often require the test material to have specific properties such as being birefringent [4] for photo-elasticity measurement or exhibiting optically detectable particle deformation for GEM measurement [10]. As such, they can only handle a very limited number of particles (typically in the order of magnitude of 100 [8] or even less for complex particles such as sands [10]). As such, experimentally it still remains a challenge to incorporate particle shape effects into the study of inter-particle force distribution. On the other hand, due to recent advances in numerical techniques, relevant investigations have also been carried out based on discrete methods. In general all discrete methods aim at simulating the kinematics of a system of particles but in two different ways: either explicitly by penalizing the inter-particle penetration based on a certain contact model, known as the (classical) discrete element method (DEM) [11], or implicitly by solving a linear complementarity problem (LCP) with non-equality constraint for all particle contacts under the limit of infinite

✉ José E. Andrade
jandrade@caltech.edu

¹ Division of Engineering and Applied Science, California Institute of Technology, Pasadena, CA 91125, USA

particle rigidity, known as the non-smooth contact dynamics (NSCD) [12]. In the rigid grain limit (which is usually the case for most granular material application [13]), these two methods have been shown to give similar results and we refer to [14] for a detailed discussion and comparison between DEM and NSCD. Such numerical techniques have been employed to characterize the inter-particle force network of granular media ranging from disk assembly in the late 90s [15, 16] to assemblies of pentagonal particles [17], elongated particles [18, 19], polyhedras [20], to assemblies composed of poly-disperse particles [21, 22] dated ten to 5 years ago, and to investigate granular pile instability based on friction mobilization analysis of particle contacts [23, 24]. However, in all current NSCD based numerical methods, usually all contact type between a certain shaped particle must be identified and be pre-built into the algorithm for contact detection and computation. As such it can only handle a system of particles with either identical and simple shape such as isotropically shaped polygons [17] or the so-called RCR particles [19], or with very limited number of elementary particle shape type (mixture of sphere and RCR particles in [25] and mixture of cube, sphere, ellipsoid and cylinder in [14]). Another general class of DEM variant method utilizes sphere (disk) clumps [26] that can handle systems of particles with different shape, however since the number of sphere (disk) needed to approximate one particle scales up dramatically fast with the change of particle shape, this method can be computationally intractable in simulating systems of complex-shaped particles. Therefore, while many granular materials commonly seen in nature such as sands are composed of particles with different and complex shape, numerically our understanding is mostly limited to particles with simple shape besides sphere (disk). More importantly, although many qualitative agreements can be found with experimental studies such as the appearance of strong and weak force network [4] and the shear-induced alignment effect on inter-particle force distribution [27], there has been no direct validation of the inter-particle force distribution computed from classical DEM or NSCD.

In summary, experimentally investigations are limited by particle property, shape and system size; while numerically these limitations become much less of an issue, the corresponding conclusions have never been directly validated. An important question to ask is, is there a numerical technique, with computationally tractable expense, that is able to capture the inter-particle force distribution among particles with different arbitrary shape? In this paper, we attempt to answer this question—we for the first time validate the ability of a newly developed DEM variant method called LS-DEM [28] on capturing the inter-particle force distribution among particles with arbitrary shape by using a recently developed experiment technique that is able to quantitatively measure inter-particle forces [29]. The paper is structured

as follows: in Sect. 2 we present the technical details of LS-DEM; in Sect. 3 we first discuss a set of experiments that allow us to measure inter-particle forces in granular materials, then introduce the corresponding numerical simulations and lastly validate LS-DEM by comparing simulation results with experiment measurements; in Sect. 4 we outline the conclusions of this study and implications for future work.

2 Comparison between LS-DEM and DEM

2.1 Introduction to LS-DEM

LS-DEM [28] works in principle just like DEM: for each particle in a system, denoted as particle i here, once knowing all forces \mathbf{f}_i acting on it, DEM (and LS-DEM) simulates its dynamics by numerically integrating Newton's equations of motion for the translational and rotational degrees of freedom:

$$m_i \frac{d^2 \mathbf{r}_i}{dt^2} = \mathbf{f}_i, \quad \text{and} \quad \frac{d}{dt} (\mathbf{I}_i \cdot \boldsymbol{\omega}_i) = \mathbf{T}_i \quad (1)$$

with the mass m_i of particle i , its position \mathbf{r}_i , the total force \mathbf{f}_i acting on it due to contacts with other particles, with boundaries or due to external body force field, the 3×3 inertia matrix \mathbf{I}_i (in 3D), its angular velocity $\boldsymbol{\omega}_i$ and the total torque \mathbf{T}_i acting on it. DEM treats each simulated particle as rigid but allows a small inter-penetration d to compute the contact force \mathbf{f}_i and moment \mathbf{T}_i based on a chosen contact model. There are many contact models developed with different level of sophistications: Hertzian or Hookean contact with particle scale damping [13, 30], incorporation of rolling resistance [31, 32], consideration of hysteresis [33] etc. A detailed introduction to various contact models can be found in [34]. In our study, the total force $\mathbf{f}^{j,i}$ (for simplicity we hereafter omit the superscript and call it \mathbf{f}) exerted by particle j to i is computed based on the following formula:

$$\mathbf{f} = \mathbf{f}_n + \mathbf{f}_t \quad (2)$$

$$\mathbf{f}_n = k_n d \hat{\mathbf{n}} \quad (3)$$

$$\mathbf{f}_t = - \frac{\Delta \mathbf{s}}{|\Delta \mathbf{s}|} \min(k_t |\Delta \mathbf{s}|, \mu_s |\mathbf{f}_n|) \quad (4)$$

where \mathbf{f}_n and \mathbf{f}_t are respectively the normal and tangential component of \mathbf{f} ; $\hat{\mathbf{n}}$ and $\Delta \mathbf{s}$ are respectively the contact normal and the accumulated tangential displacement; μ_s is the inter-particle friction coefficient; and $k_n, (k_t)$ is the normal (tangential) contact stiffness with unit of force per area.

However, unlike DEM, LS-DEM is able to compute d and the corresponding contact force and moment among particles with various shape. In LS-DEM each individual particle is represented by two quantities: a set of spatially distributed

points $\{x_1, x_2, \dots, x_n\}$ (nodes) discretizing the particle surface (called the mesh) and a discretized level set function $\phi(\mathbf{p})$ where \mathbf{p} are the grid points with color indicating the signed distance to the grain surface (negative for inside and positive for outside), as shown in Fig. 1a. Accordingly the discretized level set function $\phi(\mathbf{p})$ is scalar-valued and implicit. While $\{x_1, x_2, \dots, x_n\}$ provides the information of particle geometry, $\phi(\mathbf{p})$ gives the signed distance of a certain point \mathbf{p} to the surface of the particle which is formed by connecting $\{x_1, x_2, \dots, x_n\}$: $\phi(\mathbf{p}) > 0$ when \mathbf{p} is outside the surface, $\phi(\mathbf{p}) = 0$ when on the surface and $\phi(\mathbf{p}) < 0$ when \mathbf{p} is inside the surface. To detect contact between two particles, a master-slave approach is used, where we evaluate the value of all nodes of the master using the level-set function of the slave. If the value of the level set function is negative for any node, contact exists and force and moment are computed for each penetrating node, which are then summed to give the

total contact force and moment between the two particles, as shown in Fig. 1b. In current LS-DEM implementation the contact model becomes:

$$f_n = \sum_{z=1}^P f_{n,z} = \sum_{z=1}^P k_n d_z \hat{n}_z \tag{5}$$

$$f_t = \sum_{z=1}^P f_{t,z} = - \sum_{z=1}^P \frac{\Delta s_z}{|\Delta s_z|} \min(k_t |\Delta s_z|, \mu_s |f_{n,z}|) \tag{6}$$

where P is the total number of penetrating nodes of particle i into particle j ; $f_{n,z}$ and $f_{t,z}$ are the normal and tangential force computed at node z ; d_z , \hat{n}_z and Δs_z follow the same definition but are now computed at each node z . In this paper, however, we modify the contact model implementation to instead only consider the node with maximum penetration. By doing so, LS-DEM becomes mesh-independent in displacement controlled loading condition and converges to DEM in simulating circular particles (see ‘‘Appendix 1’’). Taking advantage of the level set function formulation, contact detection between two arbitrarily shaped particles become very trivial and require very little computational expense. For more technical details of LS-DEM, we refer to [28, 35].

3 Beyond DEM: capturing the mechanical response of granular material with arbitrarily shaped particles

In the previous section we introduced the technical details of LS-DEM. In this section, we will show the ability of LS-DEM on capturing the macro scale response and further capturing particle scale information of a system of particles with different arbitrary shape. In order to do this, we first detail the experiments that allow us to measure both the macro scale response and the particle scale information in particular the inter-particle forces, then explain our simulation setup, and lastly compare LS-DEM simulation results to experimental measurements.

3.1 Experiments: extract inter-particle forces in granular materials

Laboratory tests are carried out using a custom-built shear apparatus designed to subject a two-dimensional analogue granular assembly to (quasi-static) shear conditions [29, 36]. The shear mechanism is generated by a displacement-controlled linear actuator connected to the shear cell. Simultaneously, a vertical load σ_N is applied to the granular assembly confined in the shear cell through a dead weight loading

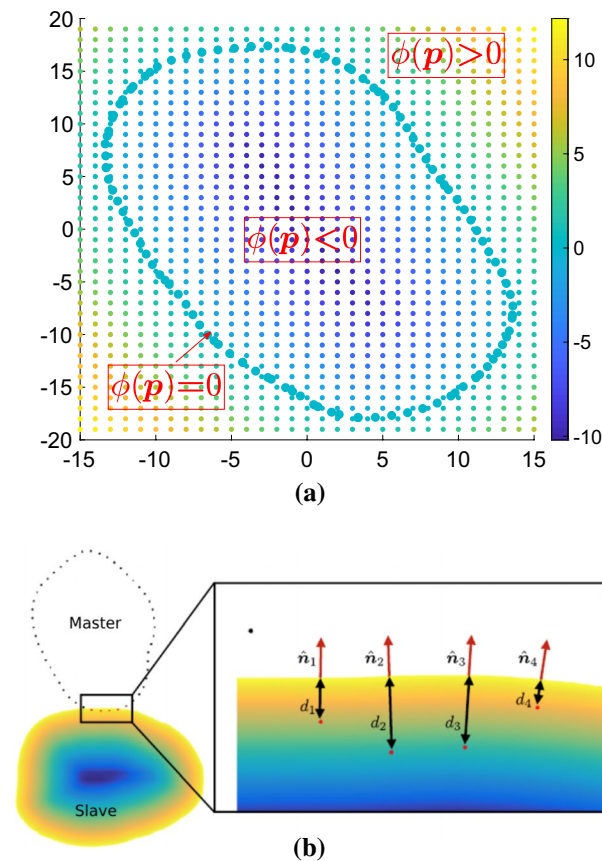


Fig. 1 a An example of constructing one particle with arbitrary shape using level set function; surface points (nodes) are shown as the dots in cyan, overlaid grid points \mathbf{p} represent the associated discretized level set function ϕ with color showing the signed distance to the surface: outside the surface $\phi(\mathbf{p}) > 0$, on the surface $\phi(\mathbf{p}) = 0$ and inside the surface $\phi(\mathbf{p}) < 0$. b Figure adapted from [35]: an example of contact detection between two particles: evaluate $\phi_s(x_i^m)$ for every node x_i^m of the master particle against the level set function ϕ_s of the slave particle (color figure online)

system. The shear cell is a horizontal deformable parallelogram with one arm fixed to a support structure and is subjected to shear strain and normal strain in the y -direction while maintaining zero normal strain in the x -direction. At each load step, image processing techniques are employed to measure the length in the y -direction L_y and shear angle θ defined as the angle between the y -axis and the tilted side of the shear cell. Given these measurements, the components of the macroscopic strain tensor ϵ are obtained as follows: $\epsilon_{xx} = 0$, $\epsilon_{yy} = \Delta L_y / L_y$ and $\epsilon_{xy} = 1/2 \tan \theta$, where ΔL_y is the change in length in the y -direction between the initial and deformed configurations. Images are acquired with an optical imaging system (Allied Vision Prosilica GT4907 15.7 Megapixel CCD camera attached to a Nikkor AF105 mm f/2.8 lens) that is installed above the apparatus (Fig. 2).

Experimental tests are performed on granular samples composed of either circular or arbitrarily-shaped grains. Both 2D analogue samples follow a log-normal distribution of grain diameter and are fabricated using the same rubber-like material (Stratasys FLX9895DM) and the same additive manufacturing technology (Stratasys Object500 Connex3 printer). All specimens were fabricated using the same additive manufacturing process. Factors such as the orientation of the print, support material composition and removal, and environmental conditions of storage of the raw materials were kept constant for all 3D-printing jobs. Such precautions were taken to ensure consistency in the effect of potential inhomogeneities and anisotropies. While the particles in the experiments have been assumed to be elastic, isotropic and homogeneous, it is clear that this is not necessarily true, and the experiments rely on averaging the two independent bulk elastic constants over several measurements and macroscopic estimates of linear elastic behavior. Quantifying the degree of inhomogeneity and

anisotropy in 3D printed materials is an open question in mechanics and lies outside the scope of our paper. Accordingly, the printed grains constituting the circular- and arbitrarily-shaped assemblies have the same mechanical properties, i.e. a Young's modulus $E = 63$ MPa and a Poisson's ratio ν of approximately 0.5. The height of the grains was set to 20 mm. The circular-shaped assembly has a total of $N_p = 313$ grains while the arbitrarily-shaped assembly is comprised of $N_p = 398$ grains. The arbitrarily-shaped assembly is engineered based on X-ray Computed Tomography images of a sand sample (Caicos ooids) [29, 37]. 11 grain shapes are extracted for their different morphological properties (i.e. sphericity and roundness). The selected grain shapes are then copied and scaled to follow a log-normal distribution. Finally, a row of circular Teflon cylinders is added between the shear cell boundaries and the granular sample to ensure that the cell is sufficiently filled.

As the sample is sheared, we perform simultaneous measurements of particle- and continuum-scale quantities that govern the mechanical behavior of granular materials. At the particle-scale, the geometrical arrangement of the granular assembly, including the position of contact points and centroids, is characterized by means of image processing (i.e. the watershed segmentation algorithm [38–40] from Matlab Image Processing Toolbox). The 2D Digital Image Correlation (2D-DIC) software VIC-2D (Correlated Solutions, Inc., Columbia, SC, USA) [41] is used to measure the intra-particle full-field displacements and strains by comparing digital images in the undeformed and deformed configurations [42, 43]. The intra-particle full-field stresses are extracted from the strains assuming Hooke's law applies. Figure 3 shows an example of the measured strain field and computed stress field for the arbitrarily shaped particle assembly at shear angle $\theta = 13.9^\circ$. The normal and tangential inter-particle forces are inferred using the Granular Element Method (GEM) [10, 36,

Fig. 2 Picture of the experimental setup

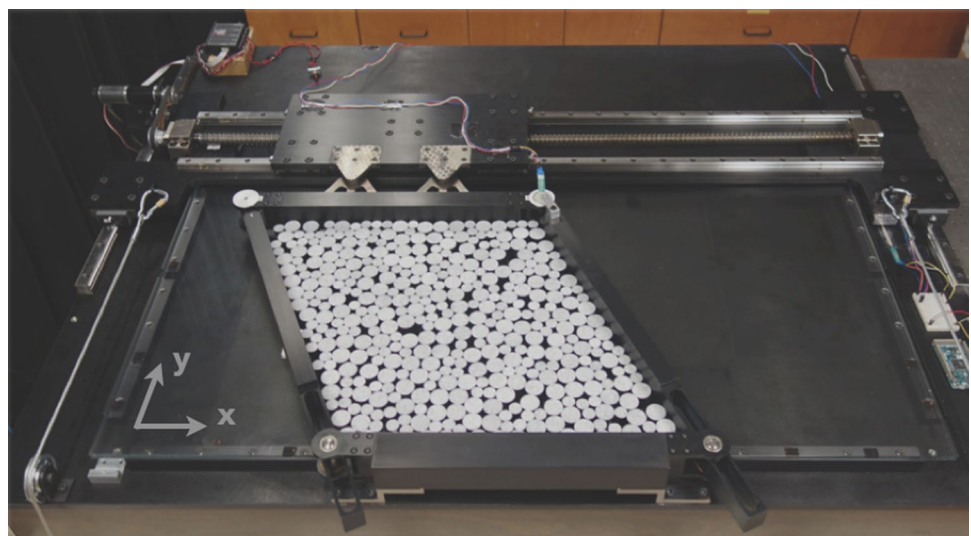
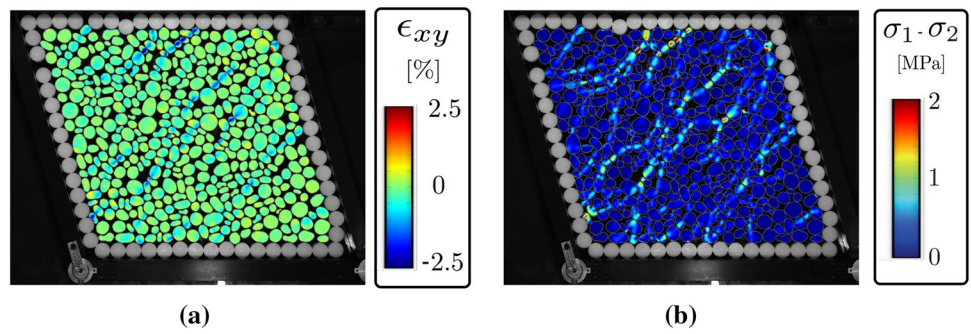


Fig. 3 **a** Measured shear strain field using DIC and **b** accordingly computed principle stress difference using the measured strain via Hooke’s law



44], provided that average particle stresses and contact point locations are known. Figure 4 presents experimental results of the intra-particle stresses and force networks obtained using the aforementioned measurement techniques at different shear angle θ in the circular- and arbitrarily-shaped assemblies.

At the macroscopic scale, the Cauchy stress tensor $\bar{\sigma}$ is expressed as a function of the inter-particle forces and fabric [45] as follows:

$$\bar{\sigma} = \frac{1}{V} \sum_{c=1}^{N_c} \text{sym} (\mathbf{f}^c \otimes \mathbf{b}^c) \tag{7}$$

where N_c is the total number of contact points, V is the total volume of the granular assembly, \mathbf{f}^c is the inter-particle force, and \mathbf{b}^c is the branch vector at the contact c .

More details on the experimental setup, granular assemblies, and measurement techniques can be found in [29, 36].

3.2 LS-DEM simulations

Since the experiments are quasi-2D, we carry out 2D LS-DEM simulations—every simulated particle has a one-to-one correspondence to the one used in the experiment, as shown in

Fig. 4 Inter-particle forces inferred with GEM superimposed on difference of principal stresses $\sigma_1 - \sigma_2$ at different values of shear angle θ for **a–c** the arbitrarily-shaped and **d–f** circular-shaped assemblies

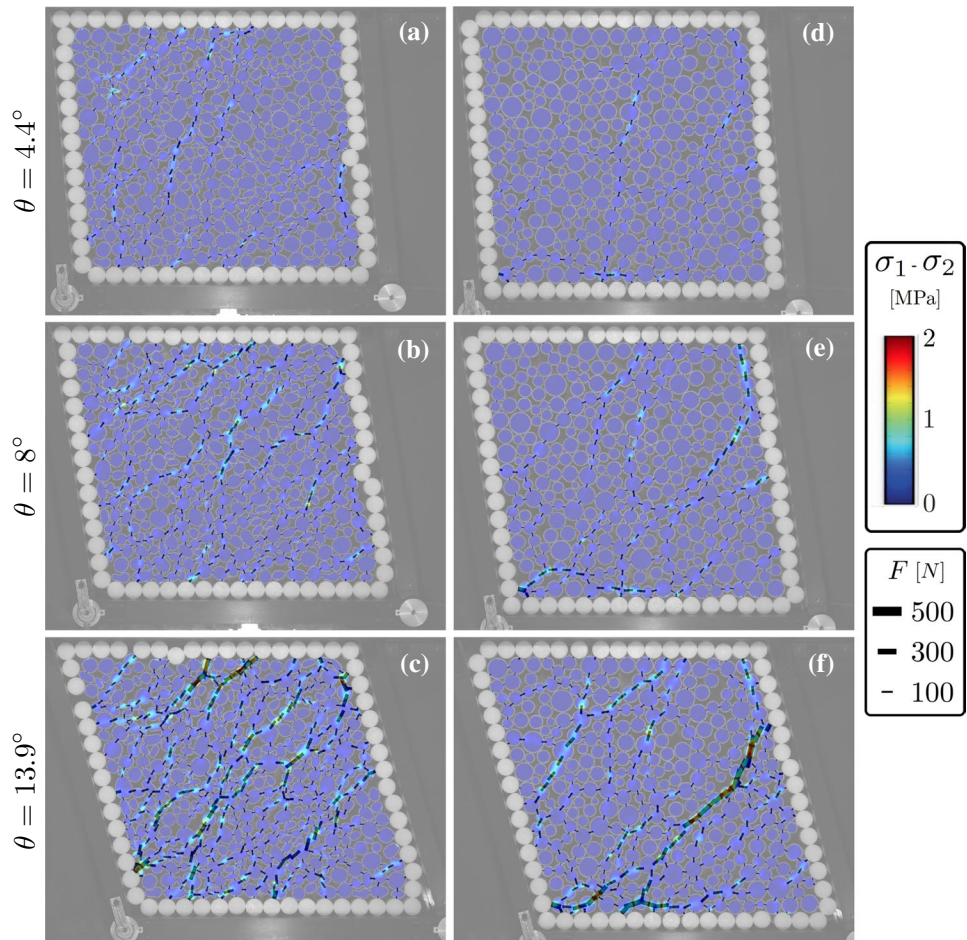


Fig. 5. In the following, based on the experimental setup, we discuss how we implement the boundary condition, choose the contact model and determine all parameters used in our simulations.

3.2.1 Boundary condition implementation

In order to properly implement the boundary boundary conditions, we start by drawing a free body diagram (Fig. 6), in which we consider the boundary frame “AD-DC-CB” without the arm “AB” which is mounted to the table and fixed. In this way, under quasi-static loading condition, “AD-DC-CB” must always be in equilibrium by balancing all external forces: forces exerted by the particles (F_{kl}), forces imposed by the weight and shear-driving motor (F_N and F_h respectively) and reaction forces at the two slider (F_A and F_B). Taking the granular assembly as a whole with one stress state, firstly we can estimate the forces exerted by the particles to the boundary as the following:

$$F_{kl} = -\sigma_\theta \cdot n_{kl} S_{kl} \tag{8}$$

where σ_θ is the 2×2 stress tensor for the granular assembly at a shear angle θ , n_{kl} and S_{kl} are respectively the normal and cross-section area of each confining bar with $kl = AD, DC$

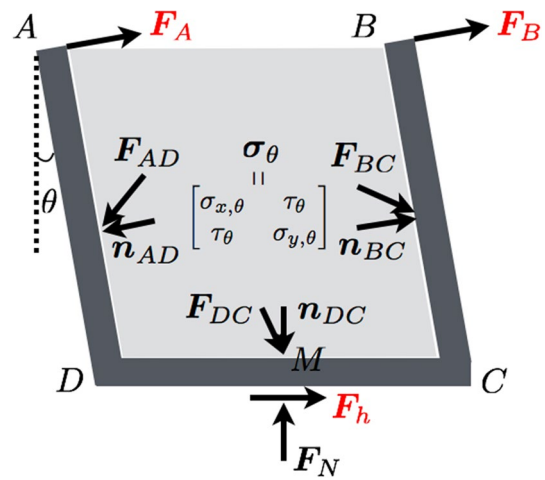
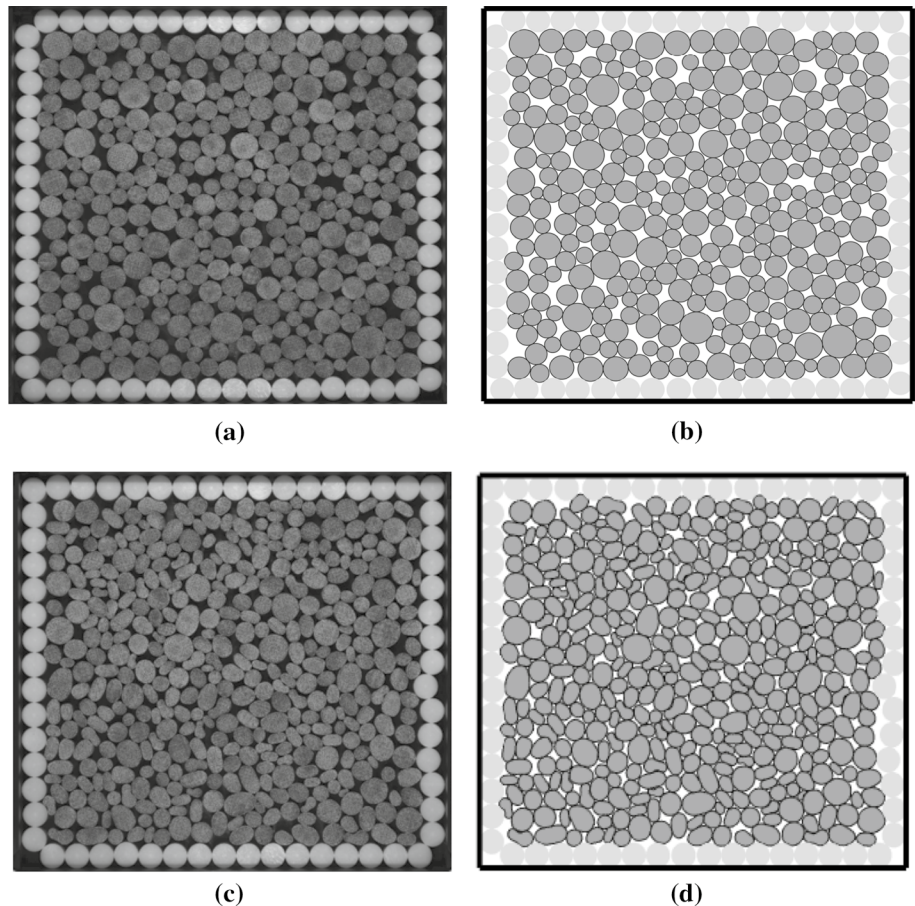


Fig. 6 Free body force diagram of the boundary frame “AD-DC-CB”; F_A , F_B and F_h are not directly measured from experiment

or BC . By force equilibrium we can solve for F_A , F_B and F_h , all of which cannot be measured in our experiments (see “Appendix 2”). In our implementation, we choose to take $(|F_A| - |F_B|)\sin\theta$ as an input in addition to F_N and θ , and compute the vertical dilation ratio $\epsilon_\theta = (h_\theta - h_0)/h_0 \times 100\%$

Fig. 5 a, c Initial configuration of the set up, b, d corresponding 2D simulation setup for cylindrical particle case and arbitrarily shaped particle case; every simulated particle has a one-to-one correspondence to the one used in the experiment—same initial configuration, size, shape and density



by moving *DC* vertically based on the force equilibrium in the *y* direction, where h_θ and h_0 are respectively the heights of the arm *DC* at a given shear angle θ and at $\theta = 0$. Table 1 shows the input quantities and also the output quantities of interest.

3.2.2 Contact between cylinders with parallel axes

In section two we presented the general contact model for our LS-DEM implementation. In this section we discuss the specific expression for each parameter such as k_n . In our experimental setup, for case one each contact takes place between two cylinders with parallel axes, we use the following applicable Hertzian contact theory that allows us to express the contact force F^c in the following way [46]:

$$F^c = \frac{\pi}{4} E^* L \delta \tag{9}$$

where E^* is the effective modulus and can be determined via $1/E^* = (1 - \nu_1^2)/E_1 + (1 - \nu_2^2)/E_2$ with ν_1, ν_2, E_1, E_2 being the Poisson's ratio and elastic modulus of the two contact cylinder respectively, L is the cylinder length, and δ is the indentation depth. Approximating δ by d we accordingly determine the normal contact stiffness by:

$$k_n = \frac{\pi}{4} E^* L \tag{10}$$

This model holds for contact between a cylinder and a flat surface by treating the flat surface as a cylinder with infinite radius. We assume that such model also holds for contact between two arbitrarily shaped particles with parallel axes. In DEM common practice is to take $k_t = \beta k_n$ with $0.5 \leq \beta \leq 1$ [13, 28, 30, 35]. However, it is found that simulation results are not sensitive to the particular value of β [30], we therefore keep the same ratio as in [35] by taking $\beta = 0.9$. In this way, all parameters of the contact model can be physically defined and directly determined from experimental measurements.

3.2.3 Parameter determination

To this point, all other parameters (k_n, β, μ_s) are introduced except two: global damping ξ and time step Δt , both of which are closely tied to the implemented time integration scheme in LS-DEM. In our study, for 2D we rewrite the equations of motion considering damping and use the

centered finite difference integration scheme proposed in [47] for numerical integration:

$$m_i \ddot{\mathbf{x}}_i + \xi m_i \mathbf{v}_i = \mathbf{f}_i \tag{11}$$

$$I_i \ddot{\boldsymbol{\alpha}}_i + \xi I_i \boldsymbol{\omega}_i = \mathbf{T}_i \tag{12}$$

$$\mathbf{v}_i^{n+1/2} = \frac{1}{1 + \xi \Delta t/2} \left[(1 - \xi \Delta t/2) \mathbf{v}_i^{n-1/2} + \frac{\Delta t}{m_i} \mathbf{f}_i \right] \tag{13}$$

$$\boldsymbol{\omega}_i^{n+1/2} = \frac{1}{1 + \xi \Delta t/2} \left[(1 - \xi \Delta t/2) \boldsymbol{\omega}_i^{n-1/2} + \frac{\Delta t}{I_i} \mathbf{T}_i \right] \tag{14}$$

$$\mathbf{r}_i^{n+1} = \mathbf{r}_i^n + \Delta t \mathbf{v}_i^{n+1/2} \tag{15}$$

$$\boldsymbol{\alpha}_i^{n+1} = \boldsymbol{\alpha}_i^n + \Delta t \boldsymbol{\omega}_i^{n+1/2} \tag{16}$$

where $\mathbf{v}_i^{n+1/2}, \mathbf{v}_i^{n-1/2}, \boldsymbol{\alpha}_i^{n+1}$ and $\boldsymbol{\alpha}_i^n$ are respectively the velocities and rotational positions of particle i at different discretized time step. The global damping ξ has unit of inverse of time, and dissipates the kinetic energy of each particle as if it is immersed in viscous fluid. We note that simulations are carried out in a loading rate faster than that imposed in experiment since it is computationally very expensive to use the real quasi-static loading rate. Accordingly, the introduction of ξ allows us to maintain quasi-static numerically by quickly dissipating kinetic energy, and helps with accounting for the dissipative frictional force between particles and the underlying glass plate that is not directly modeled in our simulation. We set Δt to be a small fraction of t_{col} to maintain numerical stability, where t_{col} is the characteristic binary collision time between two particles [33]. Now the complete parameter space of our LS-DEM model is

$$\wp = [k_n, \beta, \mu_s, \Delta t, \xi] \tag{17}$$

In this parameter space, Δt and β are determined based on common DEM computation practice. We also know the contact stiffness between the 3D-printed particles from the measured Young's modulus and Poisson's ratio (see the experiment section). For the associated friction coefficient, we consult [48] where a similar rubber-like material is used for particle fabrication, and a value of 0.6 is used. We adjust 0.6 to 0.5 such that the stress component $\sigma_{y,\theta}$ under uniaxial compression before shear is applied ($\theta = 0$), matches the applied compression force F_N on the confining bar (properly scaled by the cross section of the confining bar). Here $\sigma_{y,\theta}$ is computed from the Christofferson equation using the inter-particle forces inferred by GEM. With these four parameters being constrained, the actual parameter space reduce to just ξ . We note here that, since the PTFE particles are not considered for forces computation in the experiments, the associated friction coefficient and elastic properties are not

Table 1 Simulation input and output of interest

Input	F_N θ $(\mathbf{F}_A - \mathbf{F}_B) \sin \theta$
Output	$\epsilon_\theta = \frac{(h_\theta - h_0)}{h_0} \times 100\%$

measured. We set the friction coefficient between PTFE cylinders and that between PTFE cylinder and aluminum boundary bar both to be 0.1, elastic modulus to be 0.5 GPa and Poisson’s ratio to be 0.46 based on [49]. As the 3D-printed particles has much rougher surface than those of the PTFE particles, we set the associated friction coefficient between them to be 0.5 as well. Tables 2 and 3 show values of relevant parameters used in our simulation, where ξ_1 and ξ_2 are the damping parameters determined for cylindrical particle case and arbitrarily shaped particle case respectively. Again, we note that all modeling parameters except ξ are kept as the same for both cases and are consistent with our experimental measurements. While the damping parameter ξ can not be measured experimentally, the determined ξ_1 and ξ_2 are consistent with those estimated from a structural dynamics perspective [50]: for each particle in the system, we may simplify its interaction with all other surrounding particles effectively as a linear spring-dashpot system (LSD) with corresponding stiffness $k_{eff} \sim k_n$ and damping $\xi_{eff} \sim \sqrt{k_{eff}/m}$, where k_n and m are the contact stiffness and mass of the considered particle. Since most particles in experiments are 3D printed, we estimate k_{eff} by considering the elastic property (shown in Table 2) of such material, and compute the average mass of all 3D-printed particles, which together for both case gives $\xi \sim 10^4$ —in close proximity to the determined ξ_1 and ξ_2 . We further note that due to the particle mass distribution of each experiment case is different, we expect slight discrepancies between ξ_1 and ξ_2 .

3.3 Comparison between LS-DEM simulation and experimental results

In this section we show the comparison between LS-DEM simulation and experiment results on both the macro scale and the inter-particle force level scale.

3.3.1 Macro-scale mechanical response

LS-DEM has already been shown to be able to capture the macro-scale deformation and shear-banding of real sands subjected to triaxial loading [35]. Therefore our study serves as another evaluation on the ability of LS-DEM on capturing

Table 2 Experimentally measured material properties

Material properties	Boundary (aluminum)	PTFE cylinders	3D-printed particles
Young’s modulus E (GPa)	72	0.5	0.0635
Poisson’s ratio ν	0.33	0.46	0.5
Density ρ (kg/m ³)	2700	1471	961

Table 3 Other model input parameters

Parameters	Value
L (m)	0.02
μ_s (between boundary and PTFE cylinder)	0.1
μ_s (between PTFE cylinders)	0.1
μ_s (between PTFE cylinder and 3D-printed particle)	0.5
μ_s (between 3D-printed particles)	0.5
Δt (s)	10^{-5}
β	0.9
ξ_1 (s ⁻¹) [calibrated]	1.7×10^4
ξ_2 (s ⁻¹) [calibrated]	1.1×10^4

the macro-scale response with additional results on the grain scale. As mentioned before, on the macro scale we compare two quantities: the vertical dilation ratio $\epsilon_\theta = \frac{h_\theta - h_0}{h_0} \times 100\%$ and the average stress σ_θ at a given shear angle θ computed according to Eq. 7. Figures 7 and 8 show the comparisons for ϵ_θ and the three stress components of σ_θ : $\sigma_{x,\theta}$, $\sigma_{y,\theta}$ and τ_θ for both experimental cases. Our model correctly captures not only the evolution of all three stress components with increasing θ but also the vertical dilation ratio evolution, see Figs. 7 and 8. For the arbitrarily shaped particle experiment,

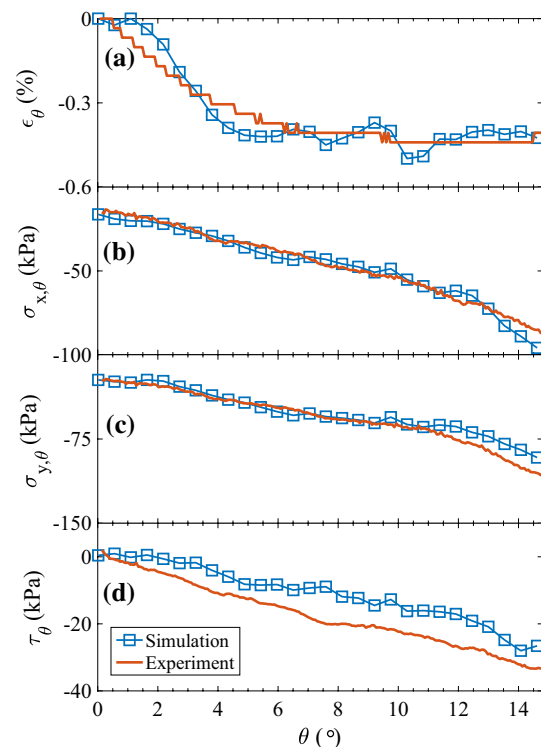


Fig. 7 Vertical dilation ϵ_θ and stress σ_θ response as the shear angle θ increases computed from experiment and simulation for the cylindrical particle case

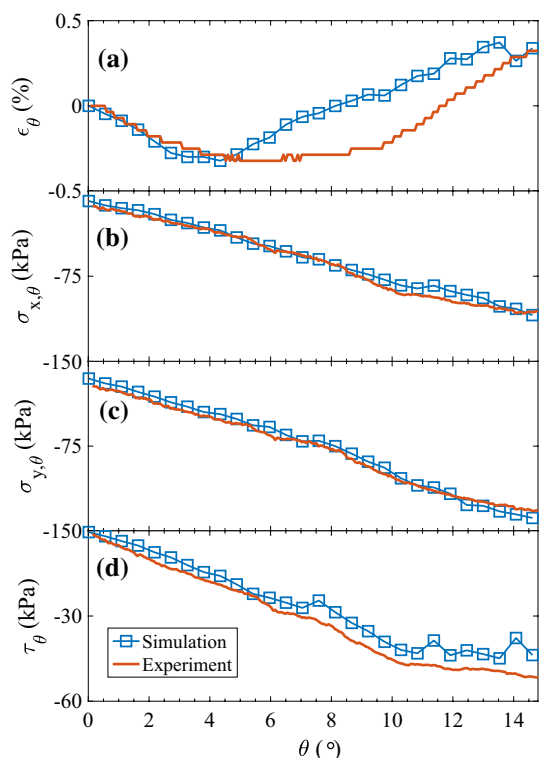


Fig. 8 Vertical dilation ϵ_θ and stress σ_θ response as the shear angle θ increases computed from experiment and simulation for the arbitrarily shaped particle case

for ϵ_θ we notice that although our model shows an earlier dilation than that from experiment, it is able to capture the overall trend and both the maximum compaction and the maximum dilation ratio at the right amount and under the right shear angle θ (Fig. 8). Our results demonstrate that by using a suitable contact model, LS-DEM is able to quantitatively capture the macro scale response of granular material with all model parameters (except the global damping ξ) being directly determined experimentally without any calibration.

3.3.2 Particle-scale force response

In this section, we go one scale downward and for the first time make comparison between experiment and simulation at the inter-particle force level. We note that, the simulations use the same physical parameters (μ_s , ν , E and ρ , see Tables 2, 3) as in the experiments. In our particular cases, we are unable to make one-to-one comparisons of kinematics and even worse kinetics at the particle level, as the particle systems are chaotic—small perturbations can create large differences. Additionally, a given contact point is sporadic and cannot be traced in time. As such, in terms of the inter-particle forces, we present qualitative and statistical comparisons. First, in terms of qualitative comparisons,

Fig. 9 show the spatial distribution of inter-particle forces for both cases in experiments and simulations at four different shear angles $\theta = 0.2^\circ, 4.4^\circ, 8.0^\circ$ and 13.9° . It can be observed that even though the exact spatial locations of large force chains are not the same between experiments and simulations, our simulations can capture the overall evolution of force network qualitatively. One step further, in terms of statistical comparisons, we compare inter-particle forces in terms of their distribution; specifically, the polar diagram of contact force magnitude $|f^c|$, the polar diagram of friction mobilization $\eta = \frac{|f^c|}{|f_n^c|}$, and the polar histogram of contact orientation defined as the direction of f_n^c (f_n^c is defined as the normal component of f^c). Figures 10 (for cylindrical particle case) and 11 (for arbitrarily shaped particle case) show the results of $|f^c|$, η and contact orientation from simulation and experiment at the same four shear angles. For all three quantities, simulations show both qualitative and quantitative agreement with experiments. In particular, in terms of the polar diagram of contact force and polar histogram of contact normal, our model successfully captures: (1) their rotation as the shear angle θ increases, and (2) larger contact forces are less mobilized than smaller ones (Figs. 10e, h, k, 11e, h, k). We observe that, especially for the case of cylindrical particles, however, simulations slightly under-estimate the magnitude of friction mobilization η . A possible reason could be that due to manufacturing errors the 3D printed spherical particles may show slight deviation from perfect disks which are however implemented in our simulation. This explanation is consistent with the result that the arbitrarily shaped particle case shows higher friction mobilization than the spherical shaped particle case.

4 Conclusions and future outlook

This study for the first time presents systematic analysis that evaluates the ability of LS-DEM on predicting particle scale response of granular material beyond the macro-scale, and beyond simple particle shape. Our contribution can be summarized as follows:

- We show that by using the suitable contact model, LS-DEM is able to capture quantitatively the macro scale mechanical response of granular material measured from experiments, with all model parameters being physically well-defined and directly measured from experiments (except damping).
- We for the first time perform systematic comparison between simulation and experiment results at the particle scale. We show that LS-DEM simulations, with all model parameters being consistent with experimental measure-

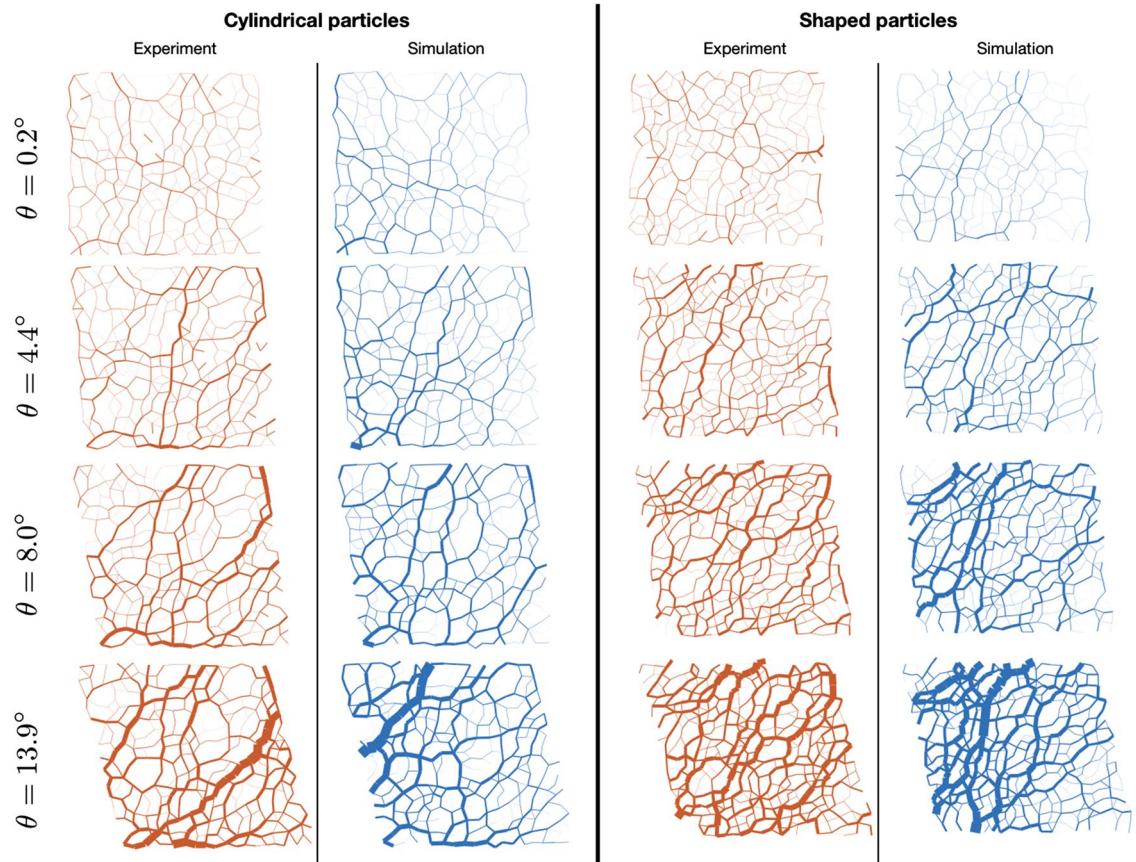


Fig. 9 The spatial distribution of inter-particle forces measured from experiments (red) and computed from simulations (blue) for both cases. All forces are shown under the same scale for a clear comparison (color figure online)

ments, can quantitatively predict the inter-particle force distribution among particles with various shape.

Our study also opens the door for several valuable future investigations. For instance, is it possible to directly determine the global damping ξ from experimental measurements? In our current implementation ξ is computed based on the average mass of the system and is held constant for each particle—this turns out to be a rather good approximation for our case since all particles have similar mass; however, this may be problematic for system with high polydispersity. It may be beneficial to consider particle scale damping that is commonly used for highly dynamical situations such as granular flow [13, 30], where the particle scale damping between two particles in contact is determined by the mass of the two particles, the coefficient of restitution e and the contact stiffness k_n . Investigations along this direction remains a topic for the future.

To conclude, by systematically comparing experiment and numerical simulation results at both macro and particle scales, we show the versatility and potential of LS-DEM in studying the physics and mechanics of granular materials.

We also present several valuable future investigations on LS-DEM with the goal of multi-scale predictability. Along this direction, LS-DEM opens an avenue to efficiently study the inter-play between particle shape and inter-particle force distribution which remains vital in understanding not only many natural phenomena such as booming sand dunes [51], but also engineering granular particles for novel properties [52].

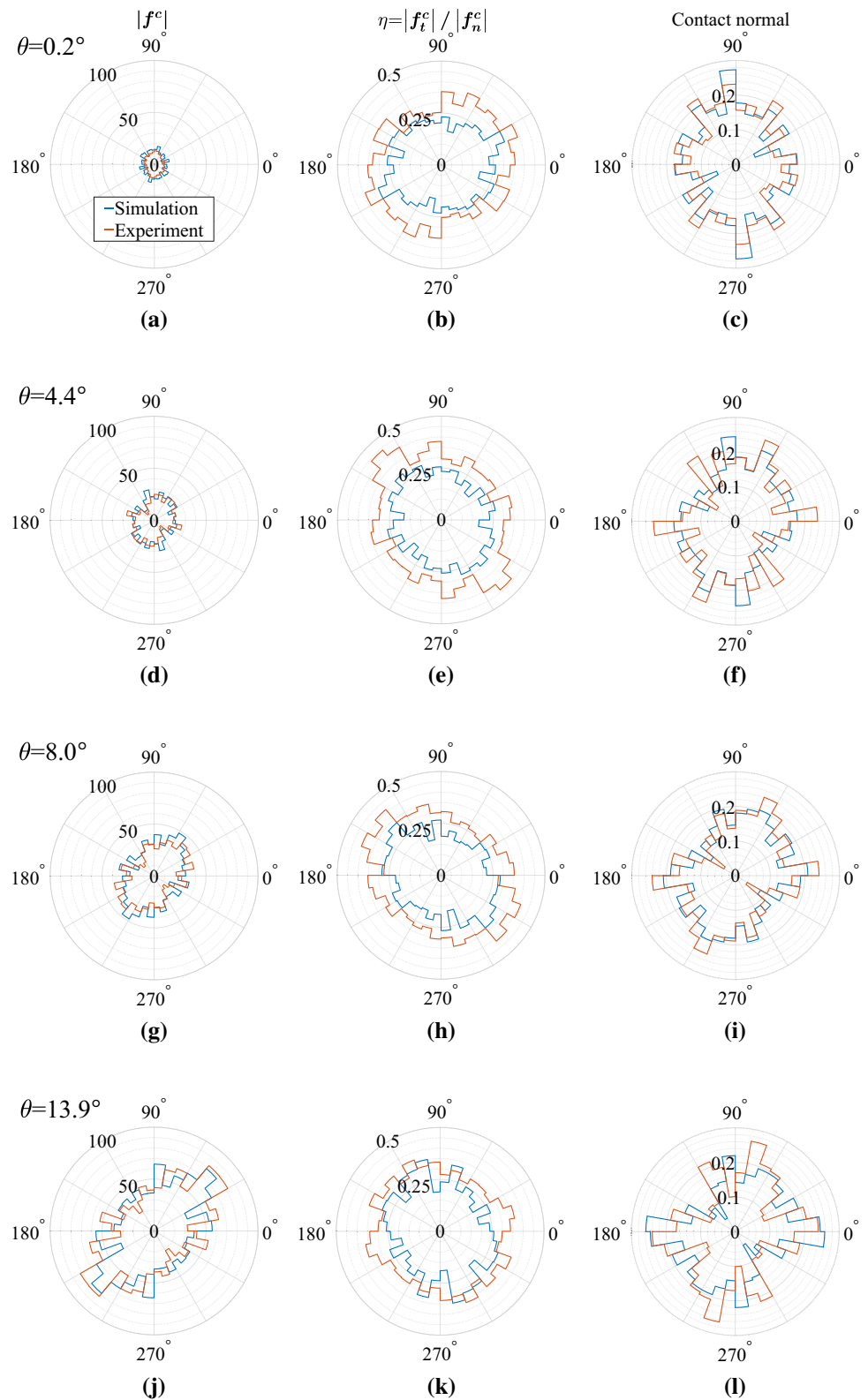
Compliance with ethical standards

Conflict of interest The authors declare that they have no conflict of interest.

Appendix 1: Resolve the mesh-dependency of current LS-DEM implementation

As mentioned in Sect. 2, in LS-DEM currently force and moment contributions from all penetrating nodes are considered, which in fact will cause LS-DEM to be mesh-dependent

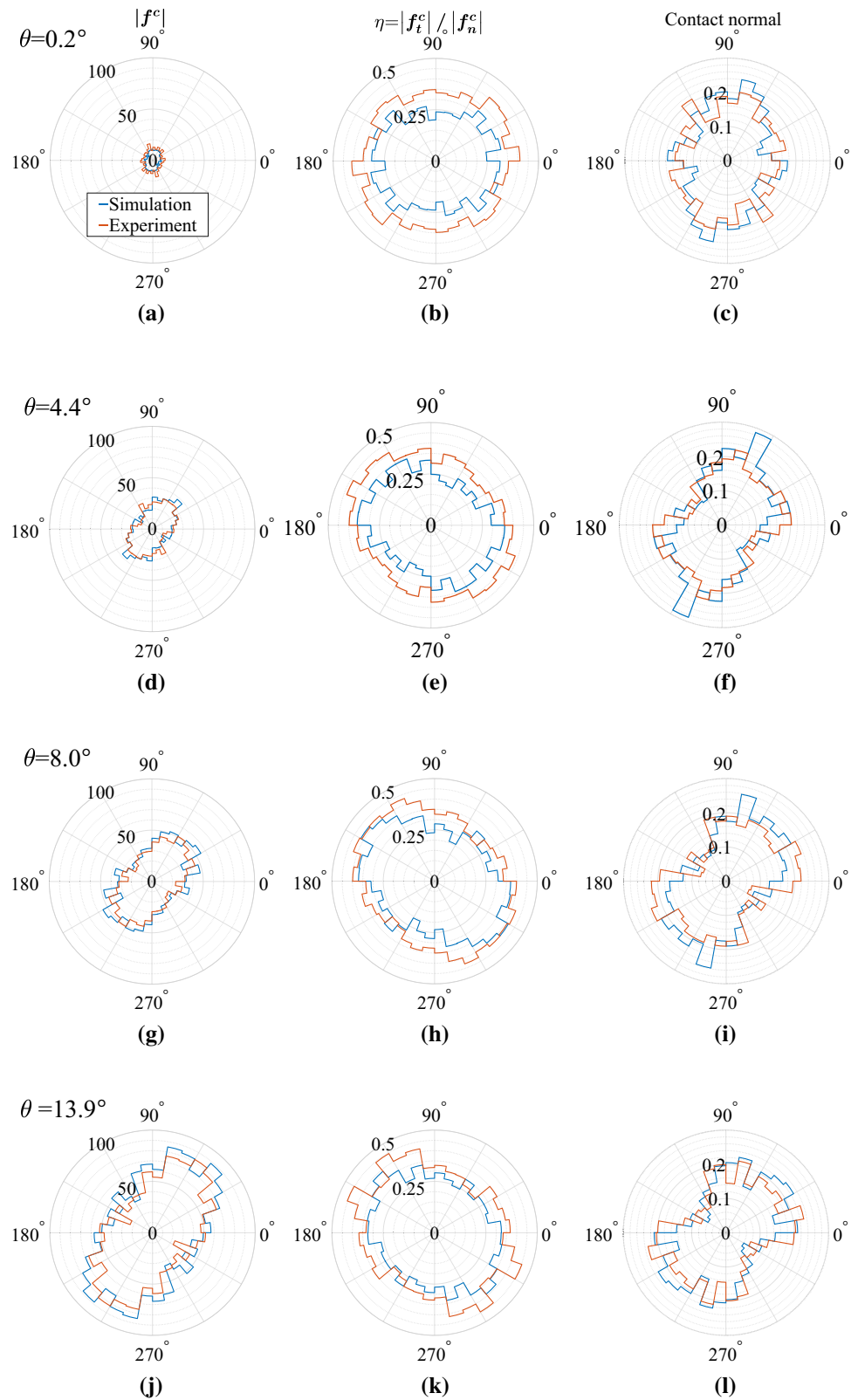
Fig. 10 Particle scale response represented by the polar diagram of contact force magnitude f^c , the polar diagram of friction mobilization $\eta = \frac{|f_t^c|}{|f_n^c|}$, and the polar histogram of contact normal at four different shear angle: $\theta = 0.2^\circ$ (a–c), $\theta = 4.4^\circ$ (d–f), $\theta = 8.0^\circ$ (g–i), and $\theta = 13.9^\circ$ (j–l) from experiment and simulation for cylindrical particle case



in displacement controlled loading condition - the mechanical response of a particle system will depend sensitively on the discretized fineness of each particle’s surface, i.e. how many nodes each particle has. However, such mesh-dependent

behavior vanishes for force controlled loading condition. To see this, using both LS-DEM and DEM with exactly the same model parameters we present several numerical tests of two identical frictional disk with radius $R = 15$ mm vertically

Fig. 11 Particle scale response represented by the polar diagram of contact force magnitude f^c , the polar diagram of friction mobilization $\eta = \frac{|f_t^c|}{|f_n^c|}$, and the polar histogram of contact normal at four different shear angle: $\theta = 0.2^\circ$ (a–c), $\theta = 4.4^\circ$ (d–f), $\theta = 8.0^\circ$ (g–i), and $\theta = 13.9^\circ$ (j–l) from experiment and simulation for arbitrarily-shaped particle case



stacked between two rigid walls with the top wall being moved downward via either displacement controlled (Δ) or force controlled condition (f), as shown in Fig. 12. In either case we

output two quantities: the contact force magnitude $|F|$, and the inter-particle penetration d . For DEM $d = 2R - |r_1 - r_2|$ where r_1, r_2 are the centroid position of the two particle

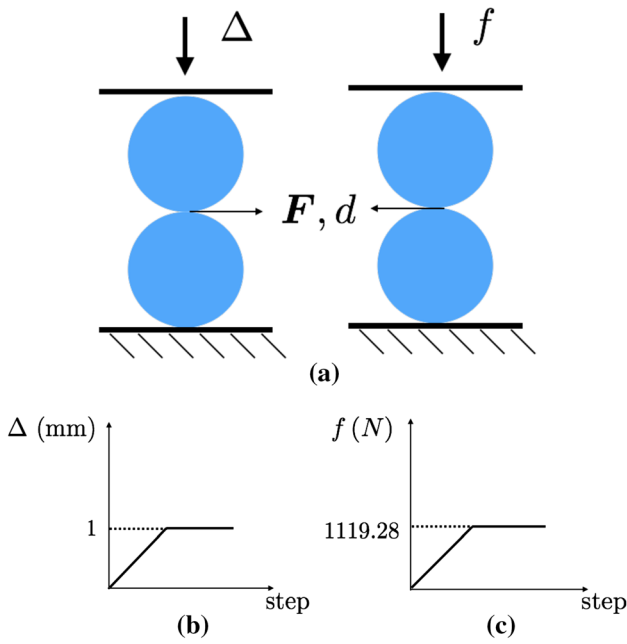


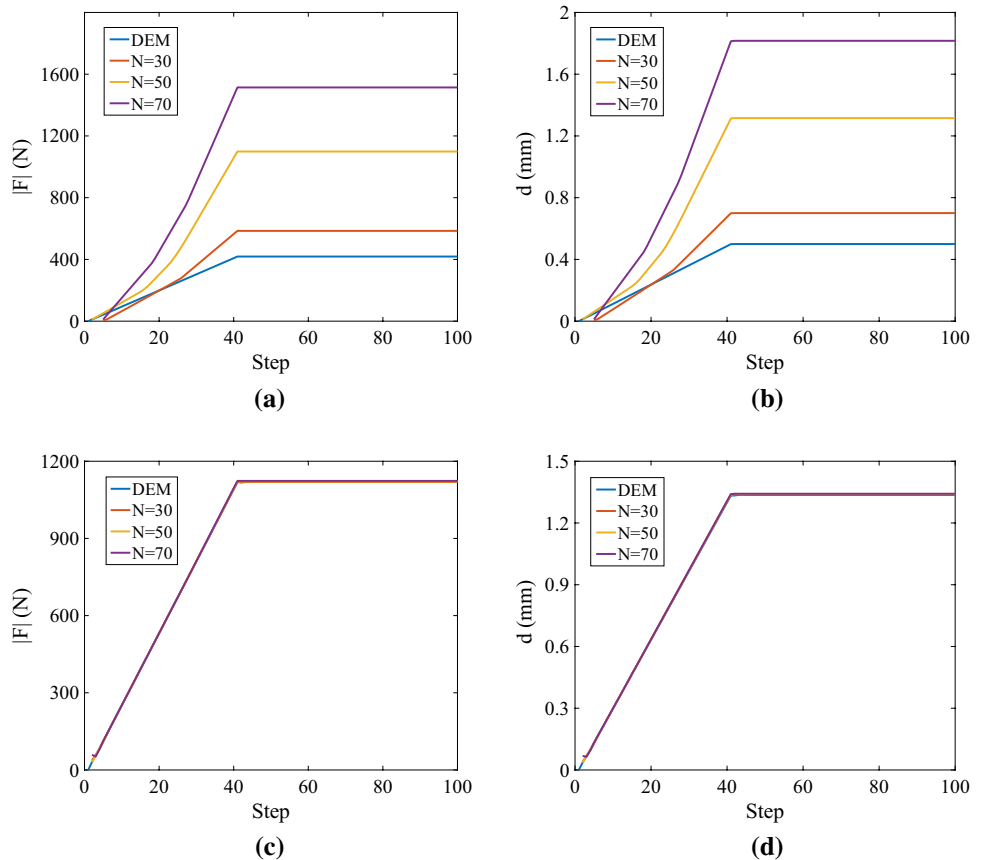
Fig. 12 a Displacement controlled and force controlled loading condition with prescribed Δ and f respectively, and both with output the inter-particle force F and penetration d ; b, c Loading curve of input Δ and f

respectively; for LS-DEM $d = \sum_z d_z$ where we sum over the penetration d_z of all penetrating nodes. For LS-DEM simulation each disk surface is randomly spatially discretized with either 30, 50 or 70 nodes. As shown in Fig. 13, the mesh-dependence problem appears for displacement controlled loading condition while vanishes for force controlled case. This can be explained by the following: in displacement controlled case the top wall is displaced downward for a certain amount that will lead to larger contact force with denser disk surface discretization, which subsequently leads to increasing $|F|$ and d ; while for the force controlled case, external force is already known and is used to compute displacement by enforcing equilibrium – no matter how dense the surface discretization is the total force from all penetrating nodes should always equilibrate the externally prescribed one. Therefore the results for $|F|$ and d all collapse onto those computed from DEM.

In order to solve this mesh-dependency problem and further show that LS-DEM converges to DEM with proper modification, two simple approaches are tested: regarding the contributions from all penetrating nodes, we either take average or only consider the one with maximum penetration:

$$f_n = \frac{1}{P} \sum_{z=1}^P f_{n,z}, \quad f_t = \frac{1}{P} \sum_{z=1}^P f_{t,z} \tag{18}$$

Fig. 13 Inter-particle force magnitude $|F|$ and penetration d response for displacement controlled case (a, b), and for force controlled case (c, d) from DEM simulation and LS-DEM simulations with 30, 50 or 70 nodes



or

$$\begin{aligned}
 f_n &= f_{n,z_m} \Big|_{d_{z_m}} = \max_{1 \leq z \leq P} \{d_z\}, \\
 f_t &= f_{t,z_m}^{j,i} \Big|_{d_{z_m}} = \max_{1 \leq z \leq P} \{d_z\}
 \end{aligned}
 \tag{19}$$

As shown in Fig. 14, for displacement controlled loading condition, both approaches resolve the mesh-dependency problem but only the modification of considering maximum penetration can further make LS-DEM converge to DEM: the computed $|F|$ and d from LS-DEM converge to those computed from DEM as the node number N discretizing a grain surface is increased from 30 to 70. We can expect that as N goes larger and larger, LS-DEM will converge to DEM for simulating circular particles with exactly the same model parameters.

Appendix 2: Boundary condition implementation

Here we discuss our methodology in estimating the variation of $|F_A|$ and $|F_B|$ as θ increases. We note first that all quantities mentioned here are experimentally measured. Following the

discussion in Sect. 3 (Fig. 6), we assume the forces exerted by the particles and from F_N to the boundary “AD-DC-BC” all act at the center of each bar and the former can be estimated based on the stress state of the granular assembly σ_θ . In each configuration with a certain θ value, we have the following unknown vectors: F_A , F_B and F_h , see Fig. 6. However, we only end up having three instead of six unknowns due to our experiment setup: F_A and F_B should always be perpendicular to AD and BC, and F_h should always be horizontal. We herein denote them as F_A , F_B and F_h as the corresponding signed magnitude: if positive the force is along the assumed direction, otherwise opposite. With force and torque equilibrium we have three equations and can therefore solve for F_A , F_B and F_h . At a certain configuration with a given θ , we assume that:

$$F_A = F_A [\cos\theta \ \sin\theta], \tag{20}$$

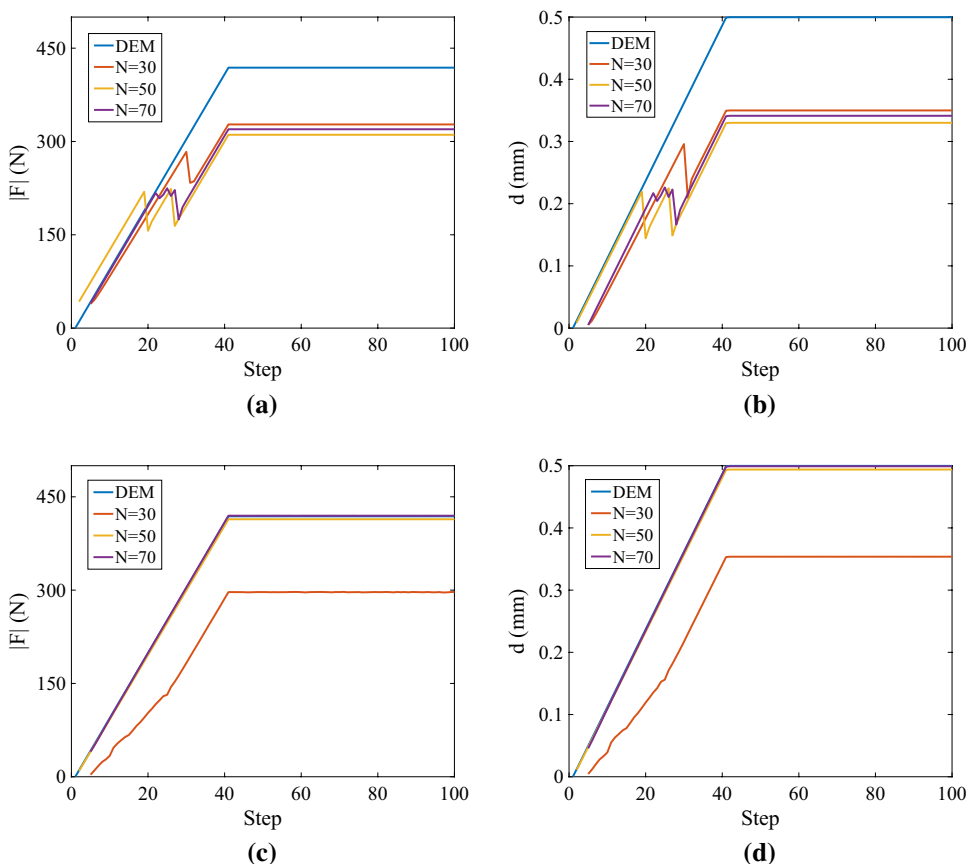
$$F_B = F_B [\cos\theta \ \sin\theta], \tag{21}$$

$$F_h = F_h [1 \ 0] \tag{22}$$

Forces exerted by the particles can be estimated by:

$$F_{pq} = -(\sigma_\theta \cdot n_{pq}) S_{pq} \tag{23}$$

Fig. 14 Inter-particle force magnitude $|F|$ and penetration d response for the same displacement controlled case from DEM simulation and LS-DEM simulations with 30, 50 or 70 nodes; **a, b** taking average for all penetrating nodes and **c, d** considering only the node with maximum penetration



where “pq” is one of “AD”, “DC” and “BC” and S_{pq} is the corresponding arm area. By force and torque equilibrium we must have:

$$\sum_l F_l = \mathbf{0} \tag{24}$$

$$\sum_l \mathbf{r}_{lM} \times F_l = \mathbf{0} \tag{25}$$

where F_l stands for all external force exerted to “AD-DC-CB” with \mathbf{r}_{lM} being the position vector point from point M (center of bar “DC”) to the location of F_l . Combining the above equations and after some algebra we arrive at the following linear system:

$$A\mathbf{u} = \mathbf{b} \tag{26}$$

where

$$A = \begin{bmatrix} \cos\theta & \cos\theta & 1 \\ \sin\theta & \sin\theta & 0 \\ A_{31} & A_{32} & 0 \end{bmatrix}, \mathbf{u} = \begin{bmatrix} F_A \\ F_B \\ F_h \end{bmatrix} \text{ and} \tag{27}$$

$$\mathbf{b} = \begin{bmatrix} \tau_\theta S_{DC} \\ \sigma_{y,\theta} S_{DC} + F_N \\ b_3 \end{bmatrix}$$

with

$$A_{31} = \frac{1}{2} \cos\theta (-2h_\theta \sec^2\theta - \mathbf{r}_{A2} + \mathbf{r}_{B2} + \tan\theta(\mathbf{r}_{A1} - \mathbf{r}_{B1})) \tag{28}$$

$$A_{32} = \frac{1}{2} \cos\theta (-2h_\theta \sec^2\theta + \mathbf{r}_{A2} - \mathbf{r}_{B2} + \tan\theta(\mathbf{r}_{B1} - \mathbf{r}_{A1})) \tag{29}$$

$$b_3 = S_{DC} [(\mathbf{r}_{A1} - \mathbf{r}_{B1}) \sin\theta \sigma_{y,\theta} + \tau_\theta (\cos\theta + \sin\theta) - (\mathbf{r}_{A2} - \mathbf{r}_{B2}) \cos\theta \sigma_{x,\theta}] \tag{30}$$

where \mathbf{r}_A and \mathbf{r}_B are locations of the slider A and B which both remain unchanged through the experiment with the subscripts “1” and “2” denote the x and y component respectively. Solving the above linear system can give us the estimation of F_A and F_B .

References

1. Richard, P., Nicodemi, M., Delannay, R., Ribiere, P., Bideau, D.: Slow relaxation and compaction of granular systems. *Nat. Mater.* **4**(2), 121 (2005)
2. Jaeger, H.M., Nagel, S.R., Behringer, R.P.: The physics of granular materials. *Phys. Today* **49**, 32–39 (1996)
3. Jaeger, H.M., Nagel, S.R., Behringer, R.P.: Granular solids, liquids, and gases. *Rev. Mod. Phys.* **68**(4), 1259 (1996)
4. Majmudar, T.S., Behringer, R.P.: Contact force measurements and stress-induced anisotropy in granular materials. *Nature* **435**(7045), 1079 (2005)
5. Iikawa, N., Bandi, M., Katsuragi, H.: Sensitivity of granular force chain orientation to disorder-induced metastable relaxation. *Phys. Rev. Lett.* **116**(12), 128001 (2016)
6. Cho, G.-C., Dodds, J., Santamarina, J.C.: Particle shape effects on packing density, stiffness, and strength: natural and crushed sands. *J. Geotech. Geoenviron. Eng.* **132**(5), 591–602 (2006)
7. Athanassiadis, A.G., Miskin, M.Z., Kaplan, P., Rodenberg, N., Lee, S.H., Merritt, J., Brown, E., Amend, J., Lipson, H., Jaeger, H.M.: Particle shape effects on the stress response of granular packings. *Soft Matter* **10**(1), 48–59 (2014)
8. Brodu, N., Dijkstra, J.A., Behringer, R.P.: Spanning the scales of granular materials through microscopic force imaging. *Nat. Commun.* **6**, 6361 (2015)
9. Hurley, R., Hall, S., Andrade, J., Wright, J.: Quantifying inter-particle forces and heterogeneity in 3d granular materials. *Phys. Rev. Lett.* **117**(9), 098005 (2016)
10. Hurley, R., Marteau, E., Ravichandran, G., Andrade, J.E.: Extracting inter-particle forces in opaque granular materials: beyond photoelasticity. *J. Mech. Phys. Solids* **63**, 154–166 (2014)
11. Cundall, P.A., Strack, O.D.: A discrete numerical model for granular assemblies. *Geotechnique* **29**(1), 47–65 (1979)
12. Jean, M.: The non-smooth contact dynamics method. *Comput. Methods Appl. Mech. Eng.* **177**(3–4), 235–257 (1999)
13. Da Cruz, F., Emam, S., Prochnow, M., Roux, J.-N., Chevoir, F.: Rheophysics of dense granular materials: discrete simulation of plane shear flows. *Phys. Rev. E* **72**(2), 021309 (2005)
14. Pazouki, A., Kwarta, M., Williams, K., Likos, W., Serban, R., Jayakumar, P., Negrut, D.: Compliant contact versus rigid contact: a comparison in the context of granular dynamics. *Phys. Rev. E* **96**(4), 042905 (2017)
15. Radjai, F., Jean, M., Moreau, J.-J., Roux, S.: Force distributions in dense two-dimensional granular systems. *Phys. Rev. Lett.* **77**(2), 274 (1996)
16. Radjai, F., Wolf, D.E., Jean, M., Moreau, J.-J.: Bimodal character of stress transmission in granular packings. *Phys. Rev. Lett.* **80**(1), 61 (1998)
17. Azéma, E., Radjai, F., Peyroux, R., Saussine, G.: Force transmission in a packing of pentagonal particles. *Phys. Rev. E* **76**(1), 011301 (2007)
18. Azéma, E., Radjai, F.: Stress-strain behavior and geometrical properties of packings of elongated particles. *Phys. Rev. E* **81**(5), 051304 (2010)
19. Azéma, E., Radjai, F.: Force chains and contact network topology in sheared packings of elongated particles. *Phys. Rev. E* **85**(3), 031303 (2012)
20. Azéma, E., Radjai, F., Saussine, G.: Quasistatic rheology, force transmission and fabric properties of a packing of irregular polyhedral particles. *Mech. Mater.* **41**(6), 729–741 (2009)
21. Azéma, E., Estrada, N., Radjai, F.: Nonlinear effects of particle shape angularity in sheared granular media. *Phys. Rev. E* **86**(4), 041301 (2012)
22. Voivret, C., Radjai, F., Delenne, J.-Y., El Youssoufi, M.S.: Multiscale force networks in highly polydisperse granular media. *Phys. Rev. Lett.* **102**(17), 178001 (2009)
23. Staron, L., Vilotte, J.-P., Radjai, F.: Preavalanche instabilities in a granular pile. *Phys. Rev. Lett.* **89**(20), 204302 (2002)
24. Staron, L., Radjai, F.: Friction versus texture at the approach of a granular avalanche. *Phys. Rev. E* **72**(4), 041308 (2005)

25. Azéma, E., Preechawuttipong, I., Radjai, F.: Binary mixtures of disks and elongated particles: texture and mechanical properties. *Phys. Rev. E* **94**(4), 042901 (2016)
26. Ferrellec, J.-F., McDowell, G.R.: A method to model realistic particle shape and inertia in dem. *Granul. Matter* **12**(5), 459–467 (2010)
27. Farhadi, S., Behringer, R.P.: Dynamics of sheared ellipses and circular disks: effects of particle shape. *Phys. Rev. Lett.* **112**(14), 148301 (2014)
28. Kawamoto, R., Andò, E., Viggiani, G., Andrade, J.E.: Level set discrete element method for three-dimensional computations with triaxial case study. *J. Mech. Phys. Solids* **91**, 1–13 (2016)
29. Marteau, E., Andrade, J.: Do force chains exist? Effect of grain shape on force transmission and mobilized strength of granular materials. *J. Mech. Phys. Solids* (2018)
30. Silbert, L.E., Ertaş, D., Grest, G.S., Halsey, T.C., Levine, D., Plimpton, S.J.: Granular flow down an inclined plane: Bagnold scaling and rheology. *Phys. Rev. E* **64**(5), 051302 (2001)
31. Ai, J., Chen, J.-F., Rotter, J.M., Ooi, J.Y.: Assessment of rolling resistance models in discrete element simulations. *Powder Technol.* **206**(3), 269–282 (2011)
32. Estrada, N., Azéma, E., Radjai, F., Taboada, A.: Identification of rolling resistance as a shape parameter in sheared granular media. *Phys. Rev. E* **84**(1), 011306 (2011)
33. Luding, S.: Introduction to discrete element methods: basic of contact force models and how to perform the micro-macro transition to continuum theory. *Eur. J. Environ. Civ. Eng.* **12**(7–8), 785–826 (2008)
34. Kruggel-Emden, H., Simsek, E., Rickelt, S., Wirtz, S., Scherer, V.: Review and extension of normal force models for the discrete element method. *Powder Technol.* **171**(3), 157–173 (2007)
35. Kawamoto, R., Andò, E., Viggiani, G., Andrade, J.E.: All you need is shape: predicting shear banding in sand with ls-dem. *J. Mech. Phys. Solids* **111**, 375–392 (2018)
36. Marteau, E., Andrade, J.: A novel experimental device for investigating the multiscale behavior of granular materials under shear. *Granul. Matter* **19**, 77 (2017)
37. Lim, K., Kawamoto, R., Andò, E., Viggiani, G., Andrade, J.: Multiscale characterization and modeling of granular materials through a computational mechanics avatar: a case study with experiment. *Acta Geotech.* **11**, 243–253 (2016)
38. Soille, P.: *Morphological Image Analysis: Principles and Applications*, 2nd edn. Springer, New York (2003)
39. Gonzalez, R., Woods, R., Eddins, S.: *Digital Image Processing using Matlab*. Pearson Prentice Hall, New Jersey (2004)
40. Russ, J.: *The Image Processing Handbook*, 5th edn. CRC Press, Boca Raton (2007)
41. Vic-2D, Reference Manual. <http://www.correlatedsolutions.com/supportcontent/Vic-2D-v6-Manual.pdf>
42. Sutton, M., Orteu, J., Schreier, H.: *Image Correlation for Shape, Motion and Deformation Measurements: Basic Concepts, Theory and Applications*. Springer, New York (2009)
43. Pan, B., Qian, K., Xie, H., Asundi, A.: Robust full-field measurement considering rotation using digital image correlation. *Meas. Sci. Technol.* **20**, 062001 (2009)
44. Andrade, J., Avila, C.: Granular element method (gem): linking inter-particle forces with macroscopic loading. *Granul. Matter* **14**, 51–61 (2012)
45. Christoffersen, J., Mehrabadi, M., Nemat-Nasser, S.: A micromechanical description of granular material behavior. *J. Appl. Mech.* **48**(2), 339–344 (1981)
46. Popov, V.L.: *Contact Mechanics and Friction*. Springer, Berlin (2010)
47. Lim, K.-W., Andrade, J.E.: Granular element method for three-dimensional discrete element calculations. *Int. J. Numer. Anal. Methods Geomech.* **38**(2), 167–188 (2014)
48. Hurley, R., Lim, K., Ravichandran, G., Andrade, J.: Dynamic inter-particle force inference in granular materials: method and application. *Exp. Mech.* **56**(2), 217–229 (2016)
49. Fluoroproducts, D.: *Teflon® ptfe fluoropolymer resin: properties handbook*. Technical Report, DuPont™ Technical Report H-37051-3 (1996)
50. Clough, R.W., Penzien, J.: *Dynamics of Structures*. Computers & Structures, Berkeley (1995)
51. Hunt, M.L., Vriend, N.M.: Booming sand dunes. *Ann. Rev. Earth Planet. Sci.* **38**, 281–301 (2010)
52. Murphy, K.A., Reiser, N., Choksy, D., Singer, C.E., Jaeger, H.M.: Freestanding loadbearing structures with z-shaped particles. *Granul. Matter* **18**(2), 26 (2016)

Publisher's Note Springer Nature remains neutral with regard to jurisdictional claims in published maps and institutional affiliations.